Research Article

Jing Zhang, Wenbin Xin*, Guoping Luo, Ruifen Wang, and Qingyong Meng

Significant Influence of Welding Heat Input on the Microstructural Characteristics and Mechanical Properties of the Simulated CGHAZ in High Nitrogen V-Alloyed Steel

https://doi.org/10.1515/htmp-2020-0003
Received Aug 28, 2019; accepted Nov 04, 2019

Abstract: The microstructural characteristics and mechanical properties of the simulated coarse grained heat affected zone (CGHAZ) in high N V-alloyed steel have been conducted under different welding heat input, characterized by the cooling time taken from 800°C to 500°C ($t_{8/5}$). The experimental results show that the microstructure is dominantly composed of lath bainite (LB) and granular bainite (GB) at $t_{8/5}$ 30 s – 90 s. The content of LB decreases with $t_{8/5}$ increasing, and that of GB increases. When $t_{8/5}$ further increases to 120 s and 180 s, the microstructure mainly consists of intragranular polygonal ferrite (IPF) and acicular ferrite (IAF). The higher $t_{8/5}$ leads to the increased content of intragranular ferrite (IGF). Meanwhile, the prior austenite grain size (PAGS) progressively increases from 56 ± 6.0 μm to 148 ± 9.9 μm as $t_{8/5}$ increases from 30 s to 180 s. Besides, EBSD analysis indicates that the fraction of high angle grain boundaries (HAGBs) is 0.570, 0.427 and 0.624, respectively, corresponding to $t_{8/5}$ 30, 90 and 180 s. Moreover, the impact toughness decreases as $t_{8/5}$ increases from 30 s to 90 s caused by the increased PAGS and GB content, and then sharply increases with $t_{8/5}$ exceeding 90 s due to the increased formation of IGF, especially IAF. Furthermore, the high nitrogen content accelerates V(C,N) precipitation, which not only inhibits the coarsening of prior austenite grains, but promotes the formation of IGF, resulting in the increased number of HAGBs and raising impact toughness.

Keywords: welding heat input; simulated CGHAZ; microstructural characteristics; impact toughness.

1 Introduction

Architectural construction nowadays tends to be large-scale, high-rise, long-span and more complicated, which is greatly depended on welding process [1–4]. The high heat input welding not only improves production efficiency but also reduces energy consumption, attracting the increased attention from metallurgists and extensively being employed in several applications. Nevertheless, the balanced combination of high strength and excellent toughness in structural steel would be seriously upset due to welding thermal cycles experiencing rapid heating (up to 100°C/s-300°C/s), high peak temperature (up to 1350°C or higher), short time incubation (1 s-3 s) and cooling to ambient temperature. During this process, the austenite grain of heat affected zone dramatically growing, especially that of CGHAZ (adjacent to the weld fusion line), leads to the formation of brittle and coarse microstructure and eventually causes poor toughness [5, 6]. Obviously, CGHAZ is one of the weakest parts in HAZ.

The impact toughness of CGHAZ in the welds is largely determined by the microstructural characteristics mainly including microstructure type and prior austenite grain size. It is well established that intragranular ferrite, especially acicular ferrite is the desirable microstructure to obtain superior toughness because the interlocked ferrite plates have different crystallographic orientation with the neighboring microstructure resulting in the high angle grain boundaries [7, 8]. The HAGBs could act as strong barriers blocking the propagation of crack or even changing its direction and thus improves the impact toughness [9–

*Corresponding Author: Wenbin Xin: School of Materials and Metallurgy, Inner Mongolia University of Science and Technology, Baotou 014010, China; Email: xwb2580zxc@163.com
Jing Zhang: School of Materials and Metallurgy, Inner Mongolia University of Science and Technology, Baotou 014010, China
Guoping Luo: School of Materials and Metallurgy, Inner Mongolia University of Science and Technology, Baotou 014010, China
Ruifen Wang: School of Materials and Metallurgy, Inner Mongolia University of Science and Technology, Baotou 014010, China
Qingyong Meng: Technical Center of HBIS Tangsteel Company, Tangshan 063000, China

Table 1: Chemical composition of the experimental steel (wt. %).

Steel	C	Si	Mn	P	S	V	N	Fe	C_{eq}	P_{cm}
VN	0.23	0.75	1.55	0.007	0.004	0.23	0.019	Bal.	0.66	0.36

11]. Moreover, the relatively larger PAGS provides more area for the formation of IGF and increases its content. However, previous literatures [6, 12–15] reported that the large PAGS probably causes the formation of M-A constituents exerting the adverse effect on toughness and the smaller PAGS brings about better toughness of CGHAZ. As the cooling rate during welding heat cycles controlled by the welding heat input (E) or the time taken from 800°C to 500°C ($t_{8/5}$) greatly affects the PAGS and decomposition of supercooled austenite [16, 17], it's essential to clarify the effect of welding heat input on prior austenite grain size and microstructural evolution, as well as the resultant toughness properties.

In addition, although several previous studies have been done on the welding properties in Nb, V and Ti single or composite microalloyed steels combined with adding nitrogen to increase the yield strength, the relationship among prior austenite grain size, microstructure type, impact toughness and welding heat input needs further investigation. Moreover, the nitrogen content was commonly controlled to approximately 100 ppm because of the accepted view that free nitrogen atoms and large micron-sized precipitates, especially titanium nitride and/or carbonitride, do harm to the impact toughness [18, 19]. However, the high N V-alloying has been employed to produce structural steel, of which the nitrogen content reaches 190 ppm. The composition design aims to promote the precipitation of vanadium carbonitrides at austenite region which tends to be heterogeneous nucleation sites for the formation of intragranular ferrite due to their lower misfit and consequently facilitates the welds toughness. Besides, the nanoscaled V(C,N) precipitated in matrix, on dislocations and at grain boundaries during cooling process greatly enhances the welds strength [20, 21]. Notably, the addition of 190 ppm nitrogen in 0.2 wt% V-alloyed steel not only accelerates the V(C,N) precipitation to a large degree avoiding the waste of V microalloy element but also yields the aging effect caused by free nitrogen atoms according to our previous investigation [4, 22].

In the present work, the correlation among welding heat input, microstructural characteristics and mechanical properties, especially the impact toughness of the simulated CGHAZ was systematically investigated in V alloyed steel with addition of 190 ppm nitrogen for the purpose of further understanding the effect of N exerted on CGHAZ. The results will be meaningful in developing high strengthened and toughened structural steel with lower production cost.

2 Materials and Methods

2.1 Materials

The chemical composition of high N V-alloyed steel is listed in Table 1. The equivalent carbon content (C_{eq}) and the welding crack susceptibility index (P_{cm}) were calculated using Eq. 1 and Eq. 2 [18]. The experimental steel was melted in a medium frequency vacuum induction furnace, cast into 39 kg ingots, and then hot forged into bars with a diameter of 20 mm at the temperature range of 950°C-1150°C. Before experiencing the simulated welding cycles, the base metal (BM) was annealed at 900°C for an hour and then furnace cooled to ambient temperature.

$$C_{eq} = C + \frac{Mn}{6} + \frac{Cr + Mo + V}{5} + \frac{Ni + Cu}{15} \quad (1)$$

$$P_{cm} = C + \frac{Si}{30} + \frac{Mn + Cu + Cr}{20} + \frac{Ni}{60} + \frac{Mo}{15} + \frac{V}{10} + 5B \quad (2)$$

2.2 Welding Simulation Procedure

The simulated welding thermal cycles with different heat input were conducted on a Gleeble-1500D thermal mechanical simulator. The specimens were cut from the annealed steel bars along the longitudinal direction, and then machined to dimensions of 10.5 mm×10.5 mm×65 mm. The welding simulation procedure was determined by using a two-dimensional Rykalin mathematical model to simulate the thermal cycle of 20 mm thick plate, as shown in Figure 1. The specimens were heated to 1350°C at 100°C/s, and then held for 1 s. The $t_{8/5}$ was chosen as 30, 60, 90, 120 and 180 s to simulate different welding heat input which was equivalent to that in-service welding of 30.5, 43.2, 52.9, 61.1 and 74.8 kJ/cm, respectively, based on their correlation exhibited as Eq. 3 [23].

$$E = d\sqrt{\frac{4\pi l\rho c t_{8/5}}{(1/(500 - T_0)^2) - (1/(800 - T_0)^2)}} \quad (3)$$

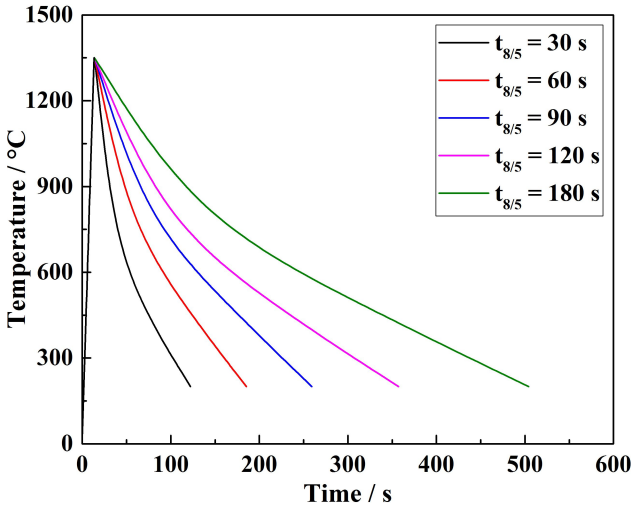

Figure 1: Welding thermal cycles applied in CGHAZ simulation for different heat input.

where E-simulated welding heat input, J; $t_{8/5}$-time taken to cool from 800°C to 500°C; l-thermal conductivity was chosen as 0.36 W/(cm·°C); ρ-density was chosen as 7.85 g/cm^3; c-specific heat capacity chosen 0.59 J/(g·°C); T_0-preheating temperature was chosen as 20°C; and d-steel thickness was chosen as 2.0 cm.

2.3 Microstructural Characterization

Metallographic specimens were cut near the monitoring thermocouple and prepared by standard techniques before being examined via an optical microscope (OM, ZEISS Axio Observer.A1m) and scanning electron microscope (SEM, JEOL JSM-6510). The measurement of average prior austenite grain size were made on micrographs of grain boundary ferrite and calculated using a linear intercept technique. More detailed microstructural examination including the morphology of microconstituents and the nanoscaled precipitated particles were performed on the thin foil and carbon replica samples using a FEI Tecnai G2 F30 transmission electron microscope (TEM). To analyze crystallographic characteristics, the simulated specimens were electrolytically polished for the observation of electron backscattered diffraction (EBSD) using auger electron spectrometer (AES, ULVAC PHI710). EBSD maps were obtained by analyzing the crystallographic information based on TSL OIM Analysis 7 software. The scanning area and step size are 160 μm × 160 μm and 0.25 μm, respectively. Meanwhile, the larger micron-sized precipitates were observed using field emission scanning electron microscope (FESEM, Zeiss Sigma 500) and the composition was determined by energy dispersion spectroscopy (EDS, Bruker).

2.4 Mechanical Properties

The specimens subjected to welding thermal cycles were machined into standard Charpy impact samples with a dimension of 10 mm×10 mm×55 mm and the notch was placed in the center of simulated CGHAZ. The impact tests were conducted on a pendulum impact testing machine (NI750) at room temperature. The fracture surfaces of the specimens were observed by using a JEOL JSM-6510 SEM.

Vickers hardness was measured at ten randomly selected regions on metallographic specimens under a load of 100 g using a THV-1MD type Vickers tester. The average values reflected the variation of microscopic hardness for the experimental steel with different welding heat input.

3 Results and Discussion

3.1 Effect of Welding Heat Input on Microstructural Evolution

The optical and scanning electron micrographs of the experimental steel in the BM and the simulated CGHAZ with different heat input are shown in Figures 2 and 3. The microstructure of BM is composed of polygonal ferrite (PF) and pearlite (P), as shown in Figures 2(a) and 3(a). At $t_{8/5}$ 30 s, the microstructure predominantly consisting of lath bainite and some fine ferrite netting along prior austenite grain boundary (PAGB) is shown in Figures 2(b) and 3(b). Laths with the same orientation got together and formed into packets and blocks while the laths with different orientations divided the prior austenite grain into different regions. From Figures 2(c) and 3(c), the microstructure at $t_{8/5}$ 60 s consists of lath bainite, granular bainite coupled with a small amount of grain boundary ferrite (GBF) and ferrite side plate (FSP) which nucleates and grows from prior austenite grain boundary to the inner grains. As $t_{8/5}$ increases to 90 s, the volume fraction of GB is obviously increased and some coarse Widmanstatten ferrite (WF) is formed from PAGB, as shown in Figures 2(d) and 3(d). Literatures [6, 24] revealed that the transformation temperature of GB and LB is similar and between the starting temperature of upper bainite and lower bainite while LB forms at a higher cooling rate compared with that of GB, which agrees with the above observed result. When $t_{8/5}$ further reaches 120 s and 180 s, the size of GBF

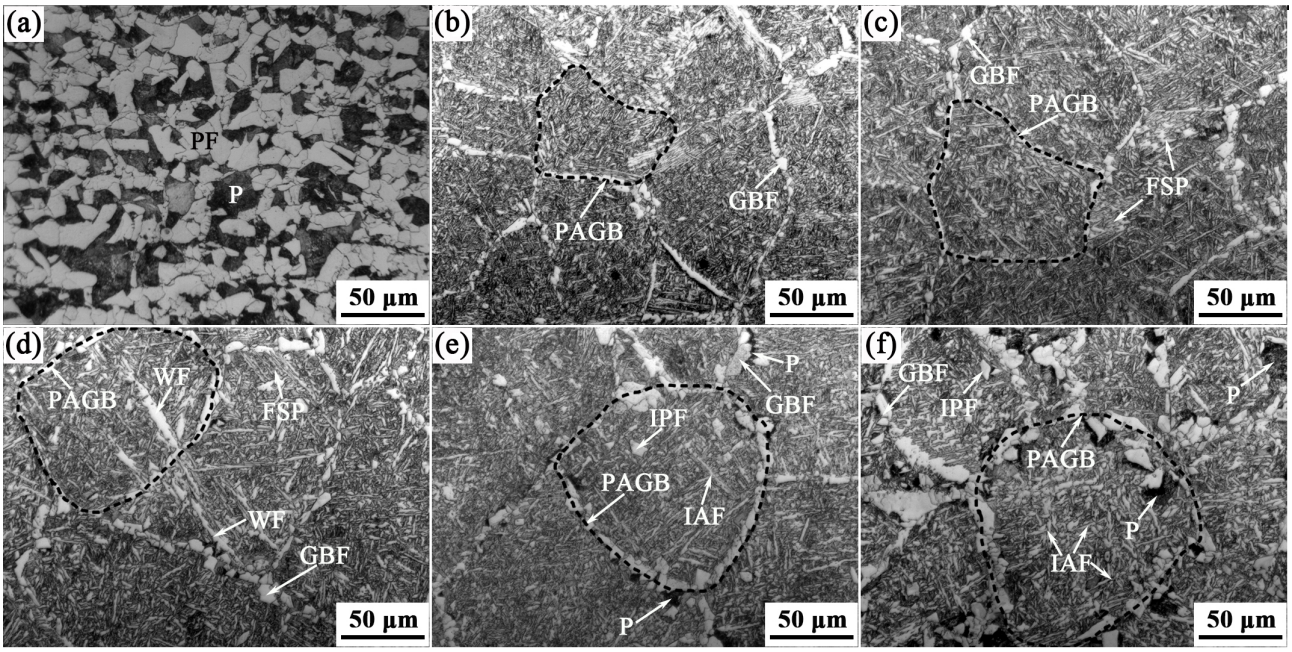

Figure 2: OM micrographs of the BM and the simulated CGHAZ at different $t_{8/5}$: (a) BM; (b) 30 s; (c) 60 s; (d) 90 s; (e) 120 s; (f) 180 s.

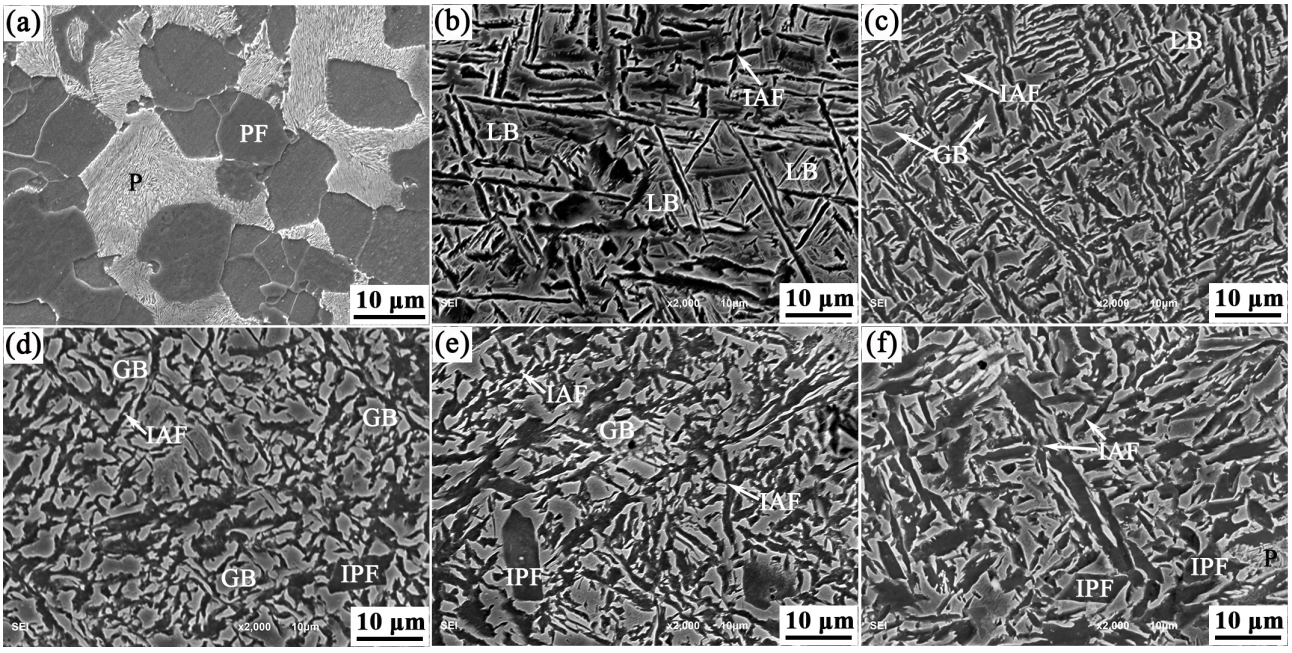

Figure 3: SEM micrographs of the BM and the simulated CGHAZ at different $t_{8/5}$: (a) BM; (b) 30 s; (c) 60 s; (d) 90 s; (e) 120 s; (f) 180 s.

is markedly increased and simultaneously the untransformed austenite will be gradually enriched with carbon, and thus the pearlite forms surrounding GBF due to local concentrated C. Moreover, the IAF and IPF generated inside of the prior austenite grains are shown in Figures 2(e), 2(f), 3(e) and 3(f), and the volume fraction of IAF and IPF is increased with $t_{8/5}$ increasing. In general, the simulated CGHAZ corresponding to $t_{8/5}$ 30 s – 90 s has bainitic dominated microstructure composed of LB and GB. The content of GB increases with $t_{8/5}$ increasing, and that of LB decreases. At $t_{8/5}$ 120 s and 180 s, the simulated CGHAZ is mainly characterized by a mixture of IAF and IPF.

As stated above, the transformed products of the simulated CGHAZ with different heat input are mostly the intermediate microstructures, including LB, GB, IAF etc., which have the complicated morphology and fine struc-

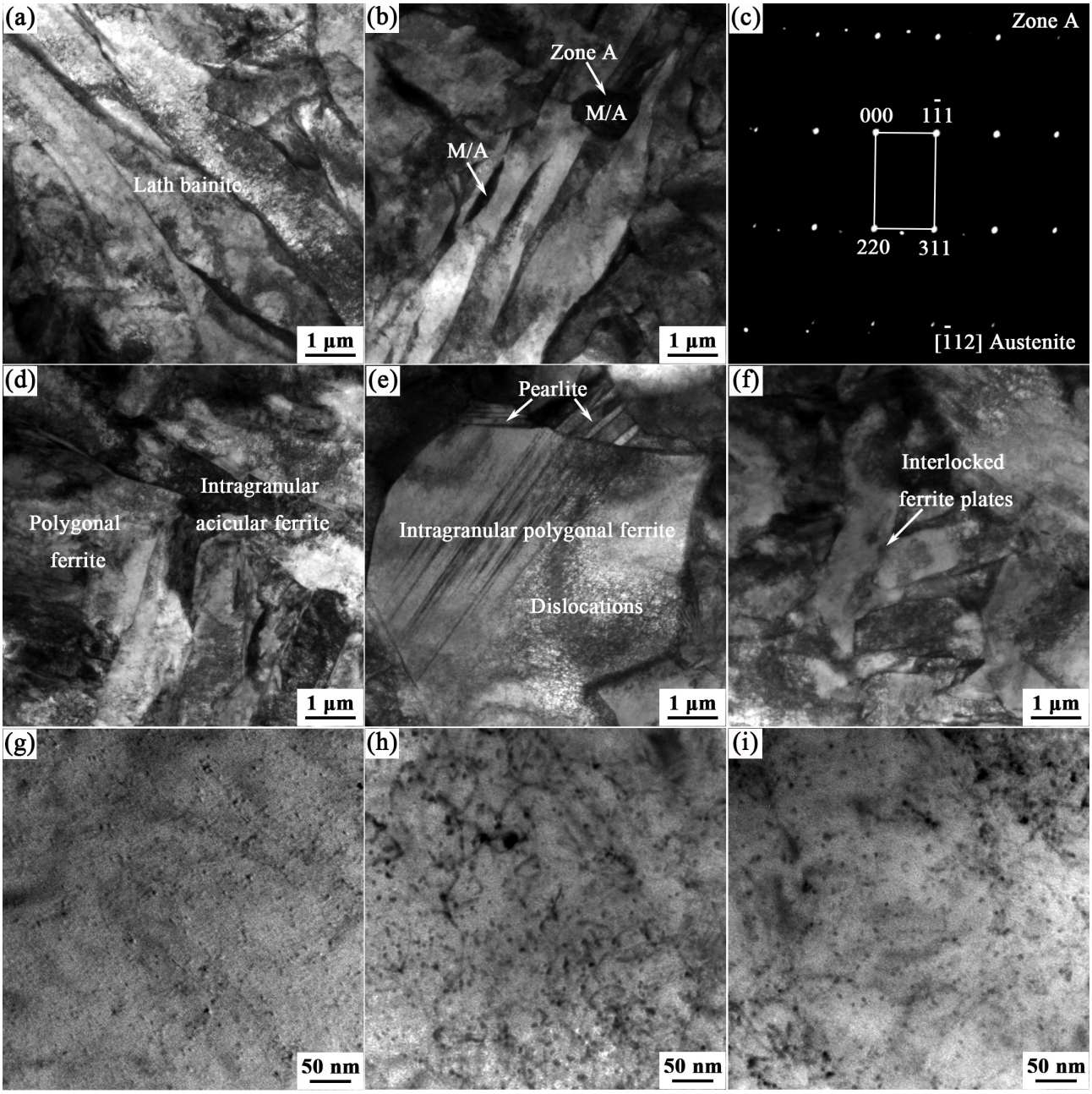

Figure 4: TEM thin foil analysis micrographs of microstructure in the simulated CGHAZ: (a) LB at $t_{8/5}$ 30 s; (b) the M/A constituents entrapped among the ferrite laths at $t_{8/5}$ 90 s; (c) the corresponding SADP for M-A island of zone A; (d) PF and IAF at $t_{8/5}$ 180 s; (e) IPF at $t_{8/5}$ 180 s; (f) IAF at $t_{8/5}$ 180 s; (g) precipitates in bainitic plates of (a); (h) precipitates in ferrite grain of (e); (i) precipitates in acicular ferrite plate of (f).

ture. More detailed microstructural features observed by TEM at typical $t_{8/5}$ for VN can be revealed as shown in Figure 4. The morphology of LB obtained at $t_{8/5}$ 30 s composed of bainitic lath structures with the same orientation is presented in Figure 4(a). For GB obtained at $t_{8/5}$ 90 s, the morphology of ferrite matrix is composed of parallel ferrite plates, as shown in Figure 4(b). Moreover, the M/A island (denoted martensite/austenite constituents) and the rod-like M/A constituents are entrapped among the ferrite plates which are harmful to the impact toughness. The corresponding selected area diffraction pattern (SADP) of zone A is presented in Figure 4(c). In Figures 4(d)-(f), the interlocked nonparallel ferrite plates with high density of dislocations termed as IAF and IPF are obtained at $t_{8/5}$ 180 s, as well as the mixed microstructure of PF and IAF. Meanwhile, some pearlite is shown adjacent to large sized fer-

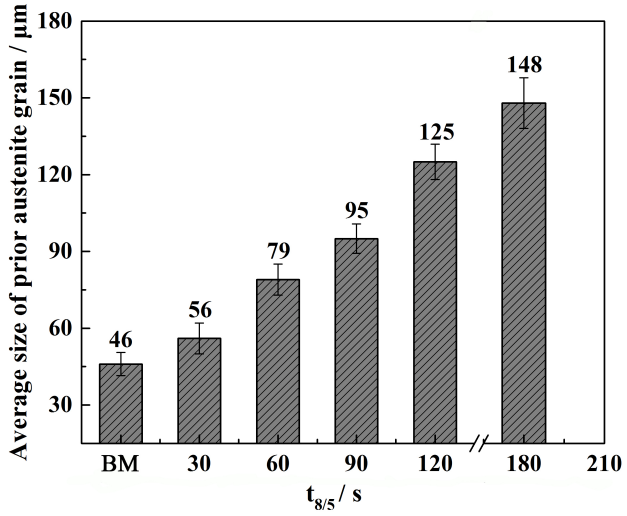

Figure 5: Prior austenite grain size of the BM and the simulated CGHAZ versus $t_{8/5}$ (The error bars represent standard deviation).

rite grain. Besides, the precipitates with small size in LB and relatively larger size in IPF and IAF are shown in Figures 4(g)-(i).

It is well acknowledged that the prior austenite grain size is largely determined to the microstructural evolution and also plays a decisive role in affecting impact toughness. Figure 5 shows the statistical PAGS of the BM and the simulated CGHAZ at different $t_{8/5}$ for the experimental steel. The PAGS of BM is 46 ± 4.5 μm and it increases from 56 ± 6.0 μm to 148 ± 9.9 μm, as $t_{8/5}$ extends from 30 s to 180 s. The PAGS is directly related to the dissolution and coarsening of microalloyed carbonitride resulting from the pinning effect of precipitates on austenite growth [23, 25, 26]. According to our previous calculation using Thermo-Calc software coupled with TCFE6 database, the precipitation temperature of V(C,N) is 1210°C [22]. During the welding thermal cycles as shown in Figure 1, the V(C,N) particles were first dissolved in the heating period and subsequently reprecipitated in the cooling process. The obvious coarsening of austenite grain occurred when precipitates are completely dissolved. That is, the PAGS is progressively increased with $t_{8/5}$ increasing due to the longer dwell time at high temperature.

3.2 Effect of Welding Heat Input on Grain Boundary Misorientation

The crystallographic characteristics of the simulated CGHAZ that experienced various welding thermal cycles for experimental steel are presented in Figure 6, including the orientation image maps, image quality maps with grain boundary misorientation distribution, and the corresponding misorientation angle distribution histograms. In the image quality maps, high angle grain boundaries are defined as having misorientation greater than 15°, and the low angle grain boundaries (LAGBs) are characterized as boundaries with misorientation between 2° and 15°. It is evident that the distribution of grain boundary misorientation exhibits bimodal characteristic which is primarily distributed in the range of 5°-20° and 40°-65°. Moreover, the fraction of HAGBs is 0.570, 0.427 and 0.624, respectively, corresponding to $t_{8/5}$ 30, 90 and 180 s. At $t_{8/5}$ 30 s, there is a high fraction of HAGBs and a small amount of coarse bainite packet consisted of several blocks with the same orientation. The high angle grain boundary appears just when LB belongs to different Bain Group [27, 28]. At $t_{8/5}$ 90 s, the grain boundary ferrite shows the HAGBs and there is high fraction of LAGBs existed in granular bainite and parallel arranged laths with same orientation. As $t_{8/5}$ further increases to 180 s, the IAF comprises interlocked structure of ferrite plates, which could divide the prior austenite grain into several regions and the neighboring ferrite plates are mostly high angle misorientation. Besides, IPF also exhibits HAGBs and thus the fraction is obviously increased at $t_{8/5}$ 180 s.

3.3 Effect of Welding Heat Input on Mechanical Properties

Figure 7 shows the Vickers hardness as a function of $t_{8/5}$ for the simulated CGHAZ and the BM in experimental steel. The hardness of BM is 238 ± 15.0 HV and that of the simulated CGHAZ decreases from 298 ± 14.9 HV to 245 ± 22.3 HV when $t_{8/5}$ increases from 30 s to 180 s. At $t_{8/5}$ 30 s, the highest hardness is mainly attributed to transformation strengthening from LB, which is undesirable due to the large discrepancy with BM. At $t_{8/5}$ 60 s and 90 s, the hardness decreases due to the formation of GB, FSP and WF, accompanying with decrease of LB. The hardness of the simulated CGHAZ at $t_{8/5}$ 30 s – 90 s are largely higher than that of BM attributed to the bainitic microstructures obtained after welding thermal cycles. At $t_{8/5}$ 120 s and 180 s, the formation of GBF largely decreases the hardness, which offsets the increase due to IAF. In fact, the hardness of base metal and weld metal should be well-matched as a result that the local stress concentration of the welding joints could be released due to the uniform deformation at each sub-region. Therefore, the suitable hardness is acquired at $t_{8/5}$ 180 s and the role of transformation strengthening from acicular ferrite supplemented by nano-scaled V(C,N)

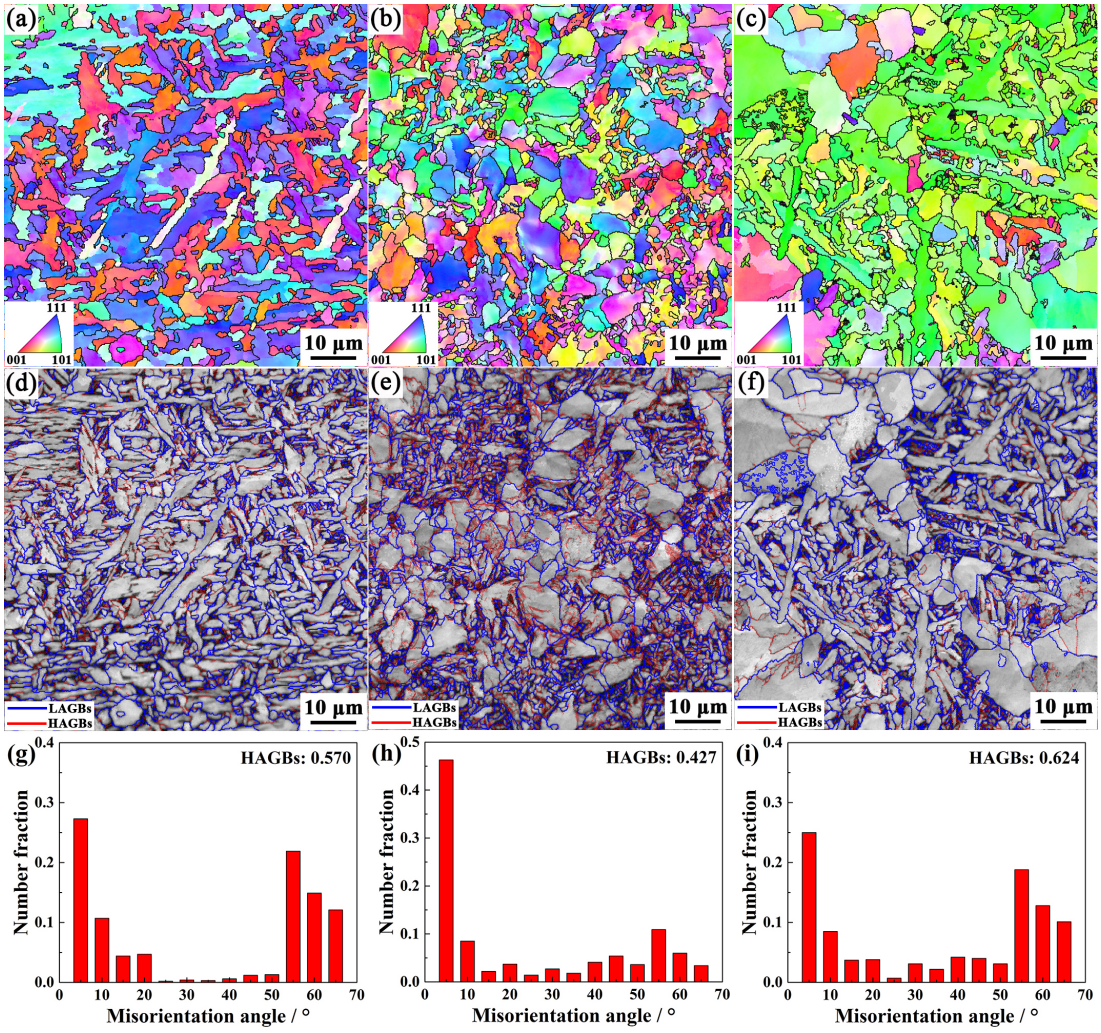

Figure 6: Crystallographic characteristics of the simulated CGHAZ at different $t_{8/5}$: (a), (d) and (g) 30 s; (b), (e) and (h) 90 s; (c), (f) and (i) 180 s; (a)-(c) orientation image maps; (d)-(f) image quality maps with grain boundary misorientation distribution (LAGBs and HAGBs are indicated by red line and blue line, respectively); and (g)-(i) misorientation angle distribution histograms.

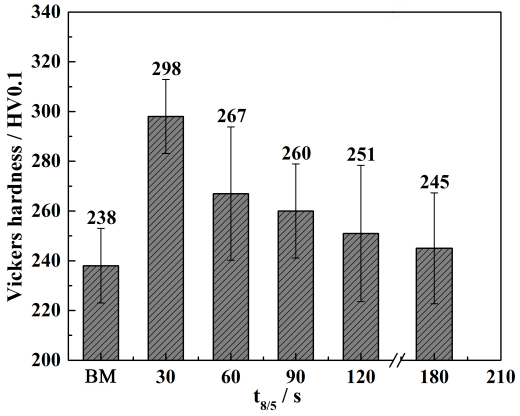

Figure 7: Vickers hardness of the BM and the simulated CGHAZ versus $t_{8/5}$ (The error bars represent standard deviation).

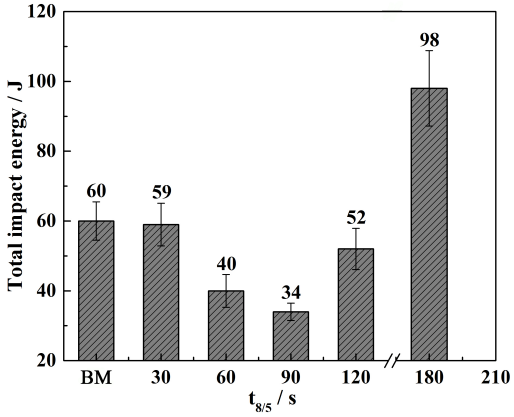

Figure 8: Total impact energy of the BM and the simulated CGHAZ versus $t_{8/5}$ (The error bars represent standard deviation).

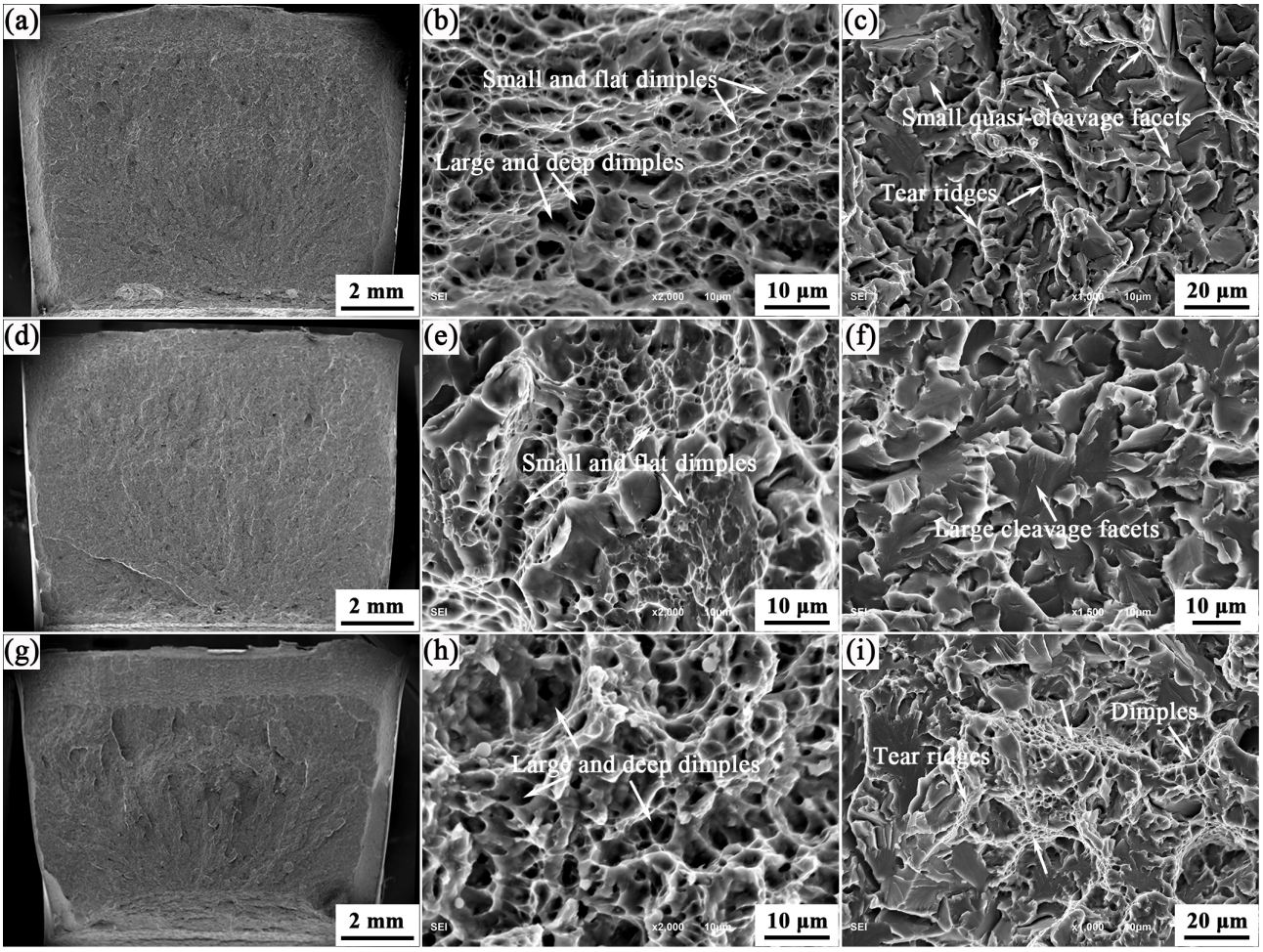

Figure 9: SEM morphologies showing impact fracture surface of the simulated CGHAZ at different $t_{8/5}$: (a)-(c) 30 s; (d)-(f) 90 s; (g)-(i) 180 s; (a), (d) and (g) macrographs; (b), (e) and (h) micrographs for ductile zone; (c), (f) and (i) micrographs for brittle zone.

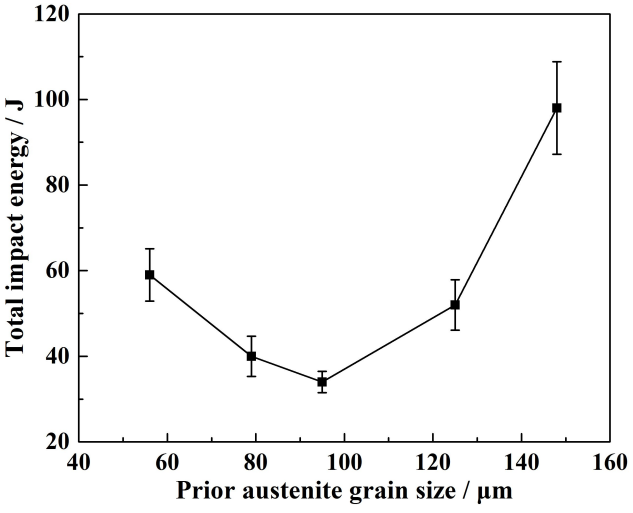

Figure 10: Total impact energy of the simulated CGHAZ as function of the prior austenite grain size.

precipitation hardening and grain boundaries strengthening make the CGHAZ hardness equivalent to that of BM.

The total impact energy of the BM and the simulated CGHAZ at different $t_{8/5}$ is presented in Figure 8. The impact energy of BM is 60 ± 5.5 J, and the value for the simulated CGHAZ is first gradually decreased from 59 ± 6.1 J to 34 ± 2.5 J as $t_{8/5}$ increases from 30 s to 90 s and then sharply increases to 98 ± 10.8 J with $t_{8/5}$ increasing to 180 s. The optimal Charpy impact toughness is obtained at $t_{8/5}$ 180 s.

The macrographs and micrographs of the impact fracture in the simulated CGHAZ at typical $t_{8/5}$ 30 s, 90 s and 180 s are shown in Figure 9. The ductile area follows the sequence of ($t_{8/5}$ = 90 s) < ($t_{8/5}$ = 30 s) < ($t_{8/5}$ = 180 s), as shown in Figures 9(a), (d) and (g). In addition, the ductile zone corresponding to $t_{8/5}$ 30 s is composed of large and deep dimples, as well as small and flat dimples, while the brittle zone is represented by small quasi-cleavage facets and some of them concatenate together by tear ridges, as revealed in Figures 9(b) and (c). From Figures 9(e) and

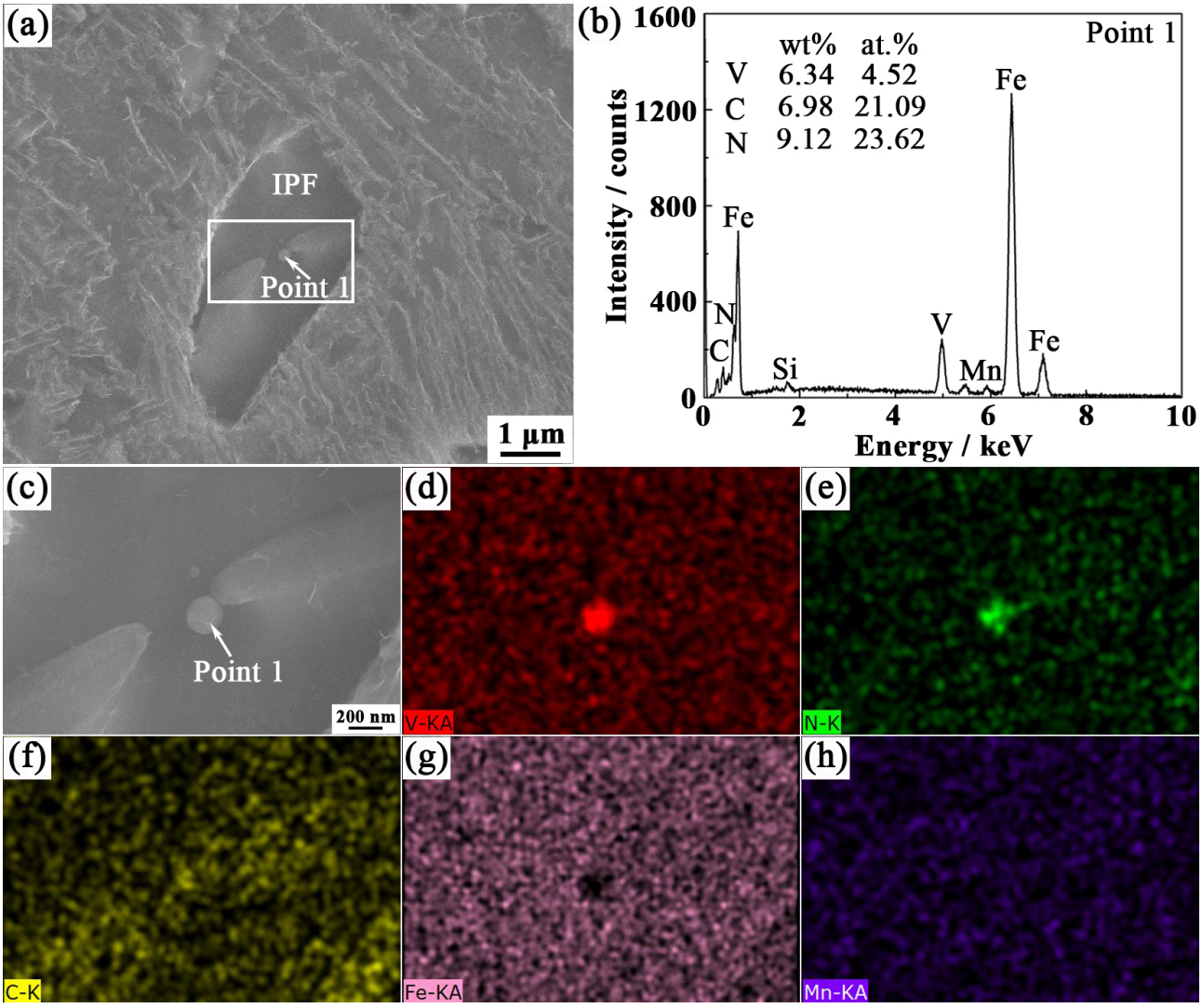

Figure 11: SEM characterization of the typical IPF and its nucleus in the simulated CGHAZ: (a) SEM image; (b) EDS spectrum; (c) magnification of marked zone in the frame; (d)-(h) EDS mapping analysis of V, N, C, Fe and Mn.

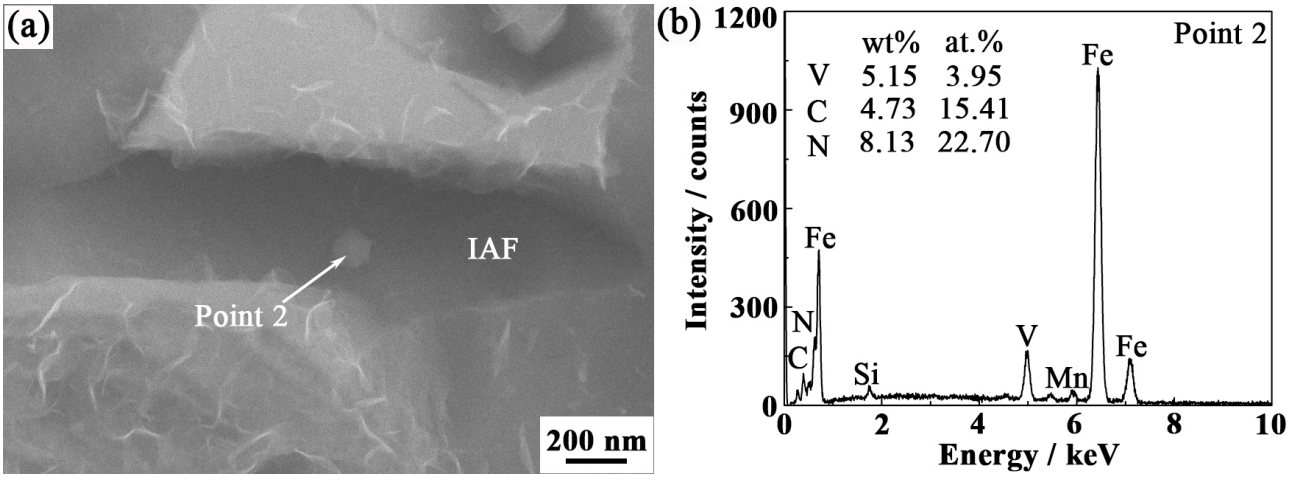

Figure 12: SEM characterization of the typical IAF and its nucleus in the simulated CGHAZ: (a) SEM image; (b) EDS spectrum.

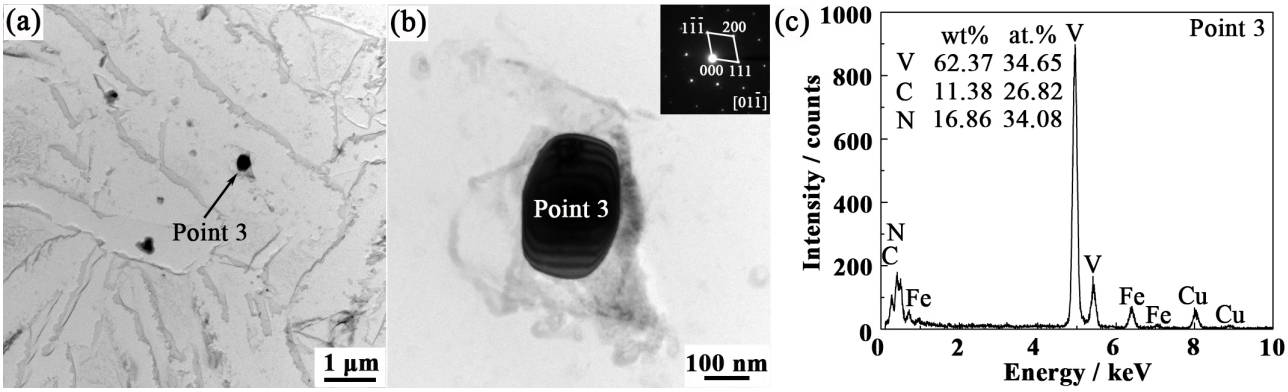

Figure 13: TEM analysis of precipitated particle in the simulated CGHAZ at $t_{8/5}$ 180 s: (a) the low magnification bright field morphology; (b) the high magnification bright field morphology inserted with SAED pattern; (c) EDS spectrum.

(f), the ductile zone for $t_{8/5}$ 90 s consists of flat dimples with different size while the brittle zone is represented by river-patterned large cleavage facets. At $t_{8/5}$ 180 s, the dimples are becoming larger and deeper in Figures 9(h) and (i). Meanwhile, the cleavage facets in brittle zone are very small and connect with dimples and tear ridges. In brief, the fracture morphology is consistent with the data obtained from impact test.

3.4 Correlation between the Microstructural Characteristics and Impact Toughness

The impact toughness of the simulated CGHAZ is largely determined by the obtained microstructural characteristics including the prior austenite grain size, microstructure type and high angle grain boundaries.

Figure 10 shows the relationship between the PAGS and the impact toughness of the simulated CGHAZ. It is evident that the total impact energy firstly decreases and then increases with the PAGS increasing. The fine PAGS commonly tends to refine the microconstituents originated from microstructure heredity and consequently improves the impact toughness [6, 15, 29], whereas it is also closely associated with the final microstructure. As the PAGS increases, the number of austenite grains per area decreases resulting in the increased intragranular area, which contributes to the formation of IGF. The transformed microstructure changes from LB+GB to IGF. Moreover, the IGF, especially IAF significantly facilitates the number of HAGBs in contrast with LB and GB. HAGBs obviously hinder the crack propagation or even change its growth direction by acting as strong barriers, remarkably consuming more energy for crack propagation. Additionally, the previous literatures [6, 30, 31] reported that the formation of coarse M/A constituents obviously causes the decrease of impact toughness. In terms of LB, GB and IGF, the optimal microstructure for excellent impact toughness of the simulated CGHAZ is intragranular ferrite, especially IAF.

The formation of IGF is not only related to the prior austenite grain size but also determined by the nucleation sites. In Figures 11(a) and 12(a), the IPF and IAF nucleate on the precipitated particles with submicron scale in the simulated CGHAZ. As shown in Figures 11(c)-(h), the elements of V and N have the same distribution characterization and the element of C is uniformly distributed in the whole region, which indicates that the nucleus is nitrogen enriched V(C,N) in combination with the EDS spectrum of Point 1 shown in Figure 11(b), as well as that of Point 2 shown in Figure 12(b). The vanadium carbonitride particles could promote the IGF formation due to the lower misfit between the precipitates and ferrite matrix [23]. In addition, an example of precipitate with a diameter of 0.27 μm detected by TEM in carbon replicas extracted from the simulated CGHAZ at $t_{8/5}$ 180s is shown in Figures 13(a) and (b). The ellipsoidal particle is also identified as N enriched V(C,N) from the corresponding EDS and SADP of Point 3 shown in Figures 13(b) and (c).

4 Conclusions

In the present study, the microstructural characteristics and mechanical properties of the simulated CGHAZ experienced various welding thermal cycles were studied in V-alloyed steel with high nitrogen content of 190 ppm. The main conclusions are as following:

(1) With $t_{8/5}$ increasing from 30 s to 180 s, the aggravated dissolution and coarsening of precipitates cause the increase of prior austenite grain size,

which leads to the microstructure type of the simulated CGHAZ changing from LB+GB to IGF.

(2) The increased content of IAF accounting for a higher fraction of HAGBs is critical to obtain the superior impact toughness in the simulated CGHAZ at $t_{8/5}$ 180 s, of which the formation is attributed to the large PAGS and the N enriched V(C,N) precipitates.

(3) The hardness of the simulated CGHAZ decreases with $t_{8/5}$ increasing. The suitable hardness is acquired at $t_{8/5}$ 180 s due to the small discrepancy with BM.

Acknowledgement: This work is financially supported by the Natural Science Foundation of China and Inner Mongolia (Grant No. 51804170, 2018BS05002), the scientific research project of higher education in Inner Mongolia autonomous region (Grant No. NJZY18144) and the program for young talents of science and technology in universities of Inner Mongolia autonomous region (Grant No. NJYT-20-B27).

References

[1] Luo, X., Y. W. Niu, X. H. Chen, H. Tang, and Z. D. Wang. High performance in base metal and CGHAZ for ferrite-pearlite steels. *Journal of Materials Processing Technology*, Vol. 242, 2017, pp. 101–109.

[2] Hutchinson, B., J. Komenda, G. S. Rohrer, and H. Beladi. Heat affected zone microstructures and their influence on toughness in two microalloyed HSLA steels. *Acta Materialia*, Vol. 97, 2015, pp. 380–391.

[3] Sugimoto, K., J. Kobayashi, and T. Hojo. Microstructure and Mechanical Properties of Ultrahigh-Strength TRIP-aided Steels. *Tetsu To Hagane*, Vol. 103, No. 1, 2017, pp. 1–7.

[4] Zhang, J., W. B. Xin, G. P. Luo, F. M. Wang, and Q. Y. Meng. Effect of the Simulated and Pilot-scaled Thermomechanical Processes on the Microstructure, Precipitates and Mechanical Properties of V–N Alloyed Steel. *ISIJ International*, Vol. 58, No. 10, 2018, pp. 1883–1892.

[5] Lan, L. Y., C. L. Qiu, D. W. Zhao, X. H. Gao, and L. X. Du. Microstructural characteristics and toughness of the simulated coarse grained heat affected zone of high strength low carbon bainitic steel. *Materials Science and Engineering A*, Vol. 529, 2011, pp. 192–200.

[6] Zhou, P. S., B. Wang, L. Wang, Y. W. Hu, and L. Zhou. Effect of welding heat input on grain boundary evolution and toughness properties in CGHAZ of X90 pipeline steel. *Materials Science and Engineering A*, Vol. 722, 2018, pp. 112–121.

[7] Seo, K., H. Ryoo, H. J. Kim, and C. Lee. Quantitative Evaluation of Nucleation Potency of Ti-containing Inclusions for Acicular Ferrite. *ISIJ International*, Vol. 59, No. 6, 2019, pp. 1105–1112.

[8] Lu, J. L., Y. P. Wang, Q. M. Wang, H. J. Cheng, and G. G. Cheng. Effect of MnS Inclusions Distribution on Intragranular Ferrite Formation in Medium Carbon Non-Quenched and Tempered Steel for Large-Sized Crankshaft. *ISIJ International*, Vol. 59, No. 3, 2019, pp. 524–530.

[9] Xiong, Z. H., S. L. Liu, X. M. Wang, C. J. Shang, X. C. Li, and R. D. K. Misra. The contribution of intragranular acicular ferrite microstructural constituent on impact toughness and impeding crack initiation and propagation in the heat-affected zone (HAZ) of low-carbon steels. *Materials Science and Engineering A*, Vol. 636, 2015, pp. 117–123.

[10] Hu, J., L. X. Du, M. Zang, S. J. Yin, Y. G. Wang, X. Y. Qi, X. H. Gao, and R. D. K. Misra. On the determining role of acicular ferrite in V-N microalloyed steel in increasing strength-toughness combination. *Materials Characterization*, Vol. 118, 2016, pp. 446–453.

[11] Shirahata, H., M. Fujioka, and K. Ushioda. Estimation of the Effective Grain Size Controlling Brittle Crack Arrest Toughness of High-strength Steel. *Tetsu To Hagane*, Vol. 104, No. 3, 2018, pp. 177–185.

[12] Gu, Y., P. Tian, X. Wang, X. L. Han, B. Liao, and F. R. Xiao. Non-isothermal prior austenite grain growth of a high-Nb X100 pipeline steel during a simulated welding heat cycle process. *Materials & Design*, Vol. 89, 2016, pp. 589–596.

[13] Bonnevie, E., G. Ferrière, A. Ikhlef, D. Kaplan, and J. M. Orain. Morphological aspects of martensite–austenite constituents in intercritical and coarse grain heat affected zones of structural steels. *Materials Science and Engineering A*, Vol. 385, No. 1-2, 2004, pp. 352–358.

[14] Lambert-Perlade, A., A. F. Gourgues, J. Besson, T. Sturel, and A. Pineau. Mechanisms and modeling of cleavage fracture in simulated heat-affected zone microstructures of a high-strength low alloy steel. *Metallurgical and Materials Transactions. A, Physical Metallurgy and Materials Science*, Vol. 35, No. 13, 2004, pp. 1039–1053.

[15] Zhu, Z., J. Han, and H. Li. Influence of Heat Input on Microstructure and Toughness Properties in Simulated CGHAZ of X80 Steel Manufactured Using High-Temperature Processing. *Metallurgical and Materials Transactions. A, Physical Metallurgy and Materials Science*, Vol. 46, No. 11, 2015, pp. 5467–5475.

[16] Kumar, S., S. K. Nath, and V. Kumar. Continuous cooling transformation behavior in the weld coarse grained heat affected zone and mechanical properties of Nb-microalloyed and HY85 steels. *Materials & Design*, Vol. 90, 2016, pp. 177–184.

[17] Lei, X. W., S. Dong, J. H. Huang, H. Yang, S. H. Chen, and X. K. Zhao. Phase evolution and mechanical properties of coarse-grained heat affected zone of a Cu-free high strength low alloy hull structure steel. *Materials Science and Engineering A*, Vol. 718, 2018, pp. 437–448.

[18] Shi, Z. R., C. F. Yang, R. Z. Wang, H. Su, F. Chai, J. F. Chu, and Q. F. Wang. Effect of nitrogen on the microstructures and mechanical properties in simulated CGHAZ of vanadium microalloyed steel varied with different heat inputs. *Materials Science and Engineering A*, Vol. 649, 2016, pp. 270–281.

[19] Zhu, Z. X., J. Han, and H. J. Li. Effect of alloy design on improving toughness for X70 steel during welding. *Materials & Design*, Vol. 88, 2015, pp. 1326–1333.

[20] Li, X. L., Z. D. Wang, X. T. Deng, Y. M. Li, H. N. Lou, and G. D. Wang. Precipitation behavior and kinetics in Nb-V-bearing low-carbon steel. *Materials Letters*, Vol. 182, 2016, pp. 6–9.

[21] Zhang, Y. J., K. Shinbo, T. Ohmura, T. Suzuki, K. Tsuzaki, G. Miyamoto, and T. Furuhara. Randomization of Ferrite/austenite Orientation Relationship and Resultant Hardness Increment by Nitrogen Addition in Vanadium-microalloyed Low Carbon Steels

Strengthened by Interphase Precipitation. *ISIJ International*, Vol. 58, No. 3, 2018, pp. 542–550.

[22] Zhang, J., F. M. Wang, Z. B. Yang, and C. R. Chang. Microstructure, Precipitation, and Mechanical Properties of V-N-Alloyed Steel After Different Cooling Processes. *Metallurgical and Materials Transactions. A, Physical Metallurgy and Materials Science*, Vol. 47, No. 12, 2016, pp. 6621–6631.

[23] Hu, J., L. X. Du, J. J. Wang, and C. R. Gao. Effect of welding heat input on microstructures and toughness in simulated CGHAZ of V–N high strength steel. *Materials Science and Engineering A*, Vol. 577, 2013, pp. 161–168.

[24] Kang, M. K., M. X. Zhang, F. Liu, and M. Zhu. Overall activation energy of isothermal transformation in metal alloy and its mechanism I. Medium temperature (bainite) isothermal transformation in steels. *Acta Metallurgica Sinica*, Vol. 45, No. 1, 2009, pp. 25–31.

[25] Zhang, L., and T. Kannengiesser. Austenite grain growth and microstructure control in simulated heat affected zones of microalloyed HSLA steel. *Materials Science and Engineering A*, Vol. 613, 2014, pp. 326–335.

[26] Moon, J., and S. H. Kim. J. B. Lee and C. H. Lee. Limiting austenite grain size of TiN-containing steel considering the critical particle size. *Scripta Materialia*, Vol. 56, 2007, pp. 1083–1086.

[27] Morris, J. W., Jr., C. S. Lee, and Z. Guo. The Nature and Consequences of Coherent Transformations in Steel. *ISIJ International*, Vol. 43, No. 3, 2003, pp. 410–419.

[28] Guo, Z., C. S. Lee, and J. W. Morris, Jr. On coherent transformations in steel. *Acta Materialia*, Vol. 52, No. 19, 2004, pp. 5511–5518.

[29] Zhu, Z. X., J. Han, H. J. Li, and C. Lu. High temperature processed high Nb X80 steel with excellent heat-affected zone toughness. *Materials Letters*, Vol. 163, 2016, pp. 171–174.

[30] Xie, H., L. X. Du, J. Hu, G. S. Sun, H. Y. Wu, and R. D. K. Misra. Effect of thermo-mechanical cycling on the microstructure and toughness in the weld CGHAZ of a novel high strength low carbon steel. *Materials Science and Engineering A*, Vol. 639, 2015, pp. 482–488.

[31] Li, C., Y. Wang, and Y. Chen. Influence of peak temperature during in-service welding of API X70 pipeline steels on microstructure and fracture energy of the reheated coarse grain heat-affected zones. *Journal of Materials Science*, Vol. 46, No. 19, 2011, pp. 6424–6431.